IOSR Journal of Applied Chemistry (IOSR-JAC)
e-ISSN: 2278-5736. Volume 18, Issue 3 Ser. 1 (March 2025), PP 49-60
www.iosrjournals.org

Visible Light Driven Dual S-scheme $BaTiO_3/BiVO_4/ZnFe_2O_4$ Nanocomposite for Methyl Orange Degradation

G. Swarupa, B. Vijaya Kumar*
Department of Chemistry, Osmania University, Hyderabad-500007, India.

Abstract
A novel $BaTiO_3/BiVO_4/ZnFe_2O_4$ (BBZ) photocatalyst was developed by depositing various weight percentages of $ZnFe_2O_4$ (5, 10,15 and 20) onto a $BaTiO_3/BiVO_4$ binary system via simple calcination method. The as-synthesized materials were analysed using various techniques, including X-ray diffraction (XRD), Fourier-transform infrared spectroscopy (FTIR), UV-visible diffuse reflectance spectroscopy (UV–vis DRS), scanning electron microscopy with energy dispersive X-ray spectroscopy (SEM-EDS), and photoluminescence (PL). These analyses confirmed the successful formation of $BaTiO_3$, $BiVO_4$, and $ZnFe_2O_4$ and their heterostructures. The bandgap energy values determined by UV–Vis DRS, suggest that the materials have the potential to function as a photocatalyst under visible light. SEM images provided insights into the morphology of the composites. The optimized BBZ-10 nanocomposite (10 wt.% $ZnFe_2O_4$) demonstrated a remarkable photocatalytic degradation of 82.4% under visible light, which is 3.43 and 3.86 times higher than pure $BaTiO_3$ (24%) and $BaTiO_3/BiVO_4$ (21.3%, respectively. Scavenger tests revealed that superoxide radicals ($\bullet O_2^-$) and hydroxyl radicals ($\bullet OH$) played a crucial role in the degradation of MO. Additionally, the stability and reusability results showed that BBZ-10 nanocomposite maintained its photocatalytic performance over four cycles, emphasizing its potential for wastewater treatment through effectively separating charge carriers and exhibiting strong degradation capability.
Keywords: *$BaTiO_3/BiVO_4/ZnFe_2O_4$, Dual S-scheme, Superoxide, Hydroxyl radicals.*

Date of submission: 14-03-2025 Date of acceptance: 27-03-2025

I. Introduction

The purification and conservation of water, along with its environmental implications, have become critical global concerns affecting human life [1]. Rapid industrialization, particularly in the textile and tannery sectors, has led to the release of harmful organic pollutants, including synthetic dyes, into water, air, and soil. Synthetic dyes such as methylene blue (MB), methyl orange (MO), rhodamine B (Rh-B), congo red (CR), and methyl red (MR) belong to a family of complex organic compounds widely used in the paint, printing, and textile industries. Dye-contaminated wastewater is the most hazardous industrial effluent, contributing to eutrophication and posing carcinogenic risks to aquatic ecosystems and human health [2,3]. To address these environmental challenges, various remediation methods have been developed. Among them, semiconductor-based photocatalysis has emerged as a promising solution due to its cost-effectiveness and eco-friendly approach, utilizing sunlight to degrade pollutants efficiently [4,5]. Over the past few decades, various strategies have been explored to enhance photocatalytic degradation efficiency. These include metal and non-metal doping, particle size and morphology modification, plasmonic and composite photocatalyst fabrication, and heterojunction construction. From these approaches, the development of different types of heterojunctions like type-I, type-II, type-III, Schottky type, Z-scheme, S-scheme etc.,[6,7] has been particularly effective in improving light absorption and minimizing electron-hole recombination in semiconductor photocatalysts, thereby significantly enhancing their photocatalytic activity. Among various heterojunctions, an S-scheme heterojunction photocatalyst [8,9] typically consists of two n-type semiconductors: a reduction photocatalyst (RP) with a negatively positioned conduction band (CB) and an oxidation photocatalyst (OP) with a positively positioned valence band (VB). In this system, charge transfer is primarily driven by the internal electric field (IEF) at the semiconductor interface. The IEF facilitates electron migration from the CB of RP to the VB of OP while simultaneously preventing continuous electron flow, thereby enhancing photocatalytic efficiency. In an S-scheme heterojunction, electrons with strong redox potential remain in the higher CB of RP, while holes stay in the lower VB of OP, enhancing charge separation and reactivity. Weaker charge carriers are transferred and consumed, forming a step-like charge transfer path. This structure significantly improves charge utilization and generates abundant reactive species for efficient contaminant degradation [10].

Advancing from the excellent separation of photo-induced electron-hole pairs, it is valuable to explore and design $BaTiO_3$-based heterojunctions to optimize the performance and stability of photocatalytic dye degradation. $BaTiO_3$ (n-type with E_g=3.2 eV) has an excellent piezoelectric property, stability, resistance to photo

corrosion, and especially the matching valence band (VB) and conduction band (CB) potential [11]. For example, S-scheme heterojunction composites with $BaTiO_3$ are $BaTiO_3$-MoS_2 [12], TiO_2-$BaTiO_3$ [13], $BaTiO_3$/g-C_3N_4 [14]etc., Selecting semiconductors with suitable energy band structures for constructing S-type heterojunctions with $BaTiO_3$ is an effective strategy to enhance photocatalytic activity. The built-in electric field formed at the interface facilitates the directional migration of photogenerated carriers, improving charge separation and boosting overall efficiency. Among Bi-based semiconductors, $BiVO_4$ (n-type) is a promising visible-light-responsive photocatalyst due to its suitable bandgap, high stability, low toxicity, and abundance. It has been extensively studied for wastewater treatment and CO_2 reduction. However, its photocatalytic performance is limited by a narrow light absorption range and high recombination of photogenerated carriers. Constructing heterojunctions offers a promising solution by improving charge separation and boosting its reductive capacity. $BiVO_4/Fe_2O_3$ [15], $BiVO_4$/tubular g-C_3N_4 [16], BiOI/$BiVO_4$ [17] etc., are some examples of S-scheme heterostructures with $BiVO_4$. Recently, spinal-type metal oxides attained great attention in photocatalysis due to their narrow band gap energy in the range of 1.8−2.1 eV, high photocatalytic behaviour, good strength, low cost, and easy magnetic separation. The spinel-type material $ZnFe_2O_4$ (n-type) has attracted considerable attention in photocatalysis because of the narrow bandgap (about 1.83 eV), high photochemical stability, and easy synthesis and appropriate CB and VB positions for redox reactions [18]. Examples of $ZnFe_2O_4$ S-scheme heterostructures include $Ag_2MoO_4/ZnFe_2O_4$ [19], $ZnFe_2O_4$/g-C_3N_4 [20], CuO/$ZnFe_2O_4$ [21]. However, over the single heterostructures, the construction of double heterostructure provides significant advantages like more abundant surface-active sites for photocatalytic reactions. Moreover, the intimate interfacial contact between two components can also improve the charge transfer and separation of photogenerated electron–hole pairs.

In this work, loading of $ZnFe_2O_4$ onto the $BaTiO_3/BiVO_4$ binary system by constructing dual S-scheme heterojunction by simple calcination method to enhance photocatalytic activity with favourable band gap alignments. This structure creates a potential gradient at the semiconductor interface, improving charge transfer and reducing electron-hole recombination. A key factor is the controlled isoenergetic charge transfer mechanism between $BaTiO_3$-$BiVO_4$ and $BiVO_4$-$ZnFe_2O_4$, which facilitates efficient charge separation. This mechanism minimizes recombination, extends exciton lifetime, and ultimately maximizes MO degradation, demonstrating the superior performance of the $BaTiO_3/BiVO_4/ZnFe_2O_4$ photocatalyst.

II. Experimental section

2.1 Materials

Potassium titanium oxalate ($K_2[TiO(C_2O_4)_2]$, 99.0%), barium chloride dihydrate ($BaCl_2.2H_2O$, 99.0%), ammonium vanadate (NH_4VO_3, 99.0%), bismuth nitrate pentahydrate ($Bi(NO_3)_3{\cdot}5H_2O$, 99.0%) were purchased from SD Fine Chemicals Ltd., sodium hydroxide (NaOH, 97%) (Merck chemicals), zinc nitrate hexahydrate ($Zn(NO_3)_2.6H_2O$, 99.0%), $Fe(NO_3)_2.9H_2O$ (98%)(Finar Chemicals), tartaric acid (99.5%), ammonium oxalate (99.0%) (Merck chemicals), tertiary butyl alcohol (>99.0%) (Merck chemicals) and benzoquinone (98.0 %) (Sigma Aldrich). All the chemicals are analytical grade and used without further purification.

2.2 Preparation of $BaTiO_3$ (BTO) by solid-state metathesis method

For the preparation of BTO, the procedure was adopted from our previous report [22]. In a typical process, the required amounts of potassium titanium oxalate and barium chloride dihydrate were dissolved separately in deionized water (DW). Then, the barium chloride solution was added to the potassium titanium oxalate solution under constant stirring for 30 min. The resultant suspension was dried on a hot plate at 30 - 40 °C for overnight. The obtained solid was ground into a fine powder and calcined in a muffle furnace at 900 °C for 24 h. After the furnace naturally cooled down to room temperature, the white powder thus obtained was treated with 0.1 M formic acid at 30 °C for 2-3 h, then washed with the DW 5-6 times to remove any unreacted barium carbonate. Finally, the samples were dried in a hot air oven at 75 °C overnight and represented as BTO throughout the manuscript.

2.3 Preparation of $BiVO_4$ (BVO) by hydrothermal method

The hydrothermal method was employed for the preparation of $BiVO_4$ [23], firstly, 1.8057 g of NH_4VO_3 was dissolved in 30 mL of DW. The solution was heated at 75 °C for 15 min until it became a clear solution. Next 7.5631 g of $Bi(NO_3)_3{\cdot}5H_2O$ was dissolved in 20 mL of DW with a few drops of conc. HNO_3. Subsequently, both solutions were combined, resulting in the formation of a light-yellow solution. The pH of the solution was adjusted to 7 by the addition of NaOH solution under constant stirring for 30 min. The precursor solution was poured into a 100 mL Teflon-lined stainless-steel autoclave for the hydrothermal treatment at 140 °C for 20 h. After cooling to room temperature, the precipitate was collected and washed several times with DW. The obtained product was dried at 60 °C for 12 h and abbreviated as BVO.

2.4 Preparation of $ZnFe_2O_4$ (ZFO) by hydrothermal method

For the preparation of ZFO, 17.1g of $Fe(NO_3)_3{\cdot}9H_2O$ and 6.2323g $Zn(NO_3)_2{\cdot}6H_2O$ were dissolved in 50 mL of deionized water and stirred for 30 min. After that, 12.7047g tartaric acid was added to the above-mentioned solutions and stirred for 30 min. Then NaOH solution was added and stirred for 30 min, the mixture solution was

transferred into a Teflon-lined autoclave and maintained at 180 °C for 24 h [24]. Then, the sample was collected and washed with deionized water and ethanol, and dried in a vacuum oven at 60 °C and denoted as ZFO.

2.5 Preparation of $BaTiO_3/BiVO_4$ (BTO/BVO) composite

The composite BTO/BVO was prepared as follows: 50 mg of BTO and 50 mg of BVO were dispersed in DW and sonicated for 2 h to ensure homogeneity. Then the suspension was dried at 60 °C for 6 h to remove the excess water and the resulting fine powder was calcined at 300 °C for 3 h. Later, the compound was collected and ground into fine powder for further use.

2.6 Preparation of $BaTiO_3/BiVO_4/ZnFe_2O_4$ (BBZ) ternary photocatalysts

Dual heterojunctions between BTO, BVO, and ZFO were prepared using the weight ratio method [(1-x) BTO/BVO/x ZFO] (x = 5, 10, 15, and 20 wt. %). For instance, the preparation of the BBZ-5 ternary system was as follows: 95 mg of BTO/BVO and 5 mg of ZFO were dispersed in DW water and sonicated for 2 h to get uniform distribution and dried on a hot plate to remove the excess water. The resulting fine powder was calcined at 300 °C for 3 h in a muffle furnace. Similarly, the other compositions were also prepared and abbreviated as BBZ-10 (90 wt.% BTO/BVO + 10 wt.% ZFO), BBZ-15 (85 wt.% BTO/BVO + 15 wt.% ZFO), and BBZ-20 (80 wt.% BTO/BVO + 20 wt.% ZFO).

2.7 Material characterization

The X-ray diffraction patterns (XRD) for each sample were acquired at room temperature using a Rigaku X-ray diffractometer by employing a Cu K_α radiation source (λ=1.5406 Å). The measurements encompassed the 2θ range of 10-80°, with a step size of 0.02° and scan step time of 0.33 seconds, aiming to ascertain the constituent phases. The Fourier Transform Infrared (FTIR) spectra were recorded using the IR prestige-21 instrument (Shimadzu, Japan). The spectra covered a range of 300-2000 cm^{-1} in the form of KBr pellets. A UV-visible spectrophotometer, UV-3600 (Shimadzu) was employed for measuring UV-visible diffuse Reflectance Spectra (DRS) in the range of 200–800 nm using $BaSO_4$ as the reference. The morphology and elemental composition were determined by using a field emission scanning electron microscope (FESEM) (Carl Zeiss Evo 18) with an acceleration voltage of 3 kV and energy dispersive X-ray spectra (EDX) respectively. The room temperature photoluminescence (PL) spectra of all the materials were recorded using a Fluoromax spectrophotometer.

2.7.1 Photocatalytic activity (PCA)

Methyl orange (MO), an anionic organic dye, was chosen as a model pollutant to evaluate the photocatalytic activity, with an initial concentration of 10^{-5} M, of the prepared materials under a 300W tungsten lamp (400–800 nm). A 50 mg photocatalyst sample was dispersed in 50 mL of MO solution and kept in the dark for 1 hour to establish adsorption-desorption equilibrium. At the time of light irradiation, 1 mL of 3% H_2O_2 was added to aqueous MO solution, 3 mL of aliquots were collected at regular time intervals, centrifuged at 5000 rpm for 10 minutes to remove solid residues, and analyzed using a Shimadzu UV-2600 UV-visible spectrophotometer by measuring absorbance at 464 nm. The rate of degradation can be measured by using the following equation

$$\text{Degradation } \% = \frac{C_0 - C_t}{C_0} * 100 \qquad (1)$$

where C_0 and C_t are the initial and time 't' (in min) concentrations of MO. The first-order kinetic rates of photocatalytic reaction were calculated by applying the Langmuir Hinshelwood first equation,

$$\ln\left(\frac{C_0}{C_t}\right) = -kt \qquad (2)$$

III. Results and discussions

3.1 X-ray diffraction (XRD)

The XRD patterns of all the prepared catalysts are shown in Fig. 1. Pure BTO exhibited characteristic peaks at 22.2°, 31.5°, 38.89°, 45.2°, 50.49°, 56.27° and 65.79° corresponding to the (100), (110), (111), (200), (210), (211) and (220) planes, respectively, in agreement with JCPDS No.89-1428. The asymmetric peak of 45.2° split into doublet as 45.03° (002) and 45.32° (200), conforming the tetragonal phase of BTO [22] with the space group of P4mm (99). For BVO, characteristic peaks at 18.60°, 18.94°, 28.88°, 30.47°, 34.49°, 35.14°, 39.95°, 42.40°, 46.01°, 47.21°, 50.25°, 53.22°, 55.86°, 53.42°,63.60°, 65.92° and 69.58° were assigned to the of (101), (011), (112), (001), (200), (020), (301), (015), (204), (024), (213), (411), (420), (332), (204), (501) and (224) planes, respectively [25], confirming its monoclinic structure (JCPDS No. 14-0688) with the space group I2/b [26,27]. No additional peaks were detected, indicating the phase purity. The peaks at 2θ = 29.82°, 35.2°, 42.7°, 53.07°, 56.6°, and 62.1° correspond to the (220), (311), (400), (422), (511) and (440) crystal planes of cubic ZFO (JCPDS No. 79–1150), with Fd-3m (227) point group [28]. In the BTO/BVO binary nanocomposite, the presence of diffraction peaks from both BTO and BVO confirms the successful binary heterostructure formation. As the content of ZFO increases, its peak intensity strengthens and the broadness of the peak increases compared to pure BTO suggesting the successful formation of ternary nanocomposite. The crystallite sizes were calculated by applying the Debye-Scherrer equation [29].

$$D = \frac{K\lambda}{\beta \cos\theta} \qquad (3)$$

where D is the crystalline size, K is the shape factor i.e., 0.94, λ is 0.15406 nm is the wavelength of the X-ray source, β is the full width at half maximum in radians, and θ is the peak position in radians. The crystallite sizes are BTO (41.5), BVO (29.2), ZFO (18), BTO/BVO (32.9), BBZ-5 (42.8), BBZ-10 (38.6), BBZ-15 (41.1) and BBZ-20 (42.3 nm). By the introduction of ZFO material to the binary system by weight ratio method will quenches the aggregation and reduces the crystallite sizes. That leads to increase in surface area and hence, developing the photocatalytic activity. The unit cell of BTO, BVO and ZFO drawn from VESTA software, shown in Fig. 2.

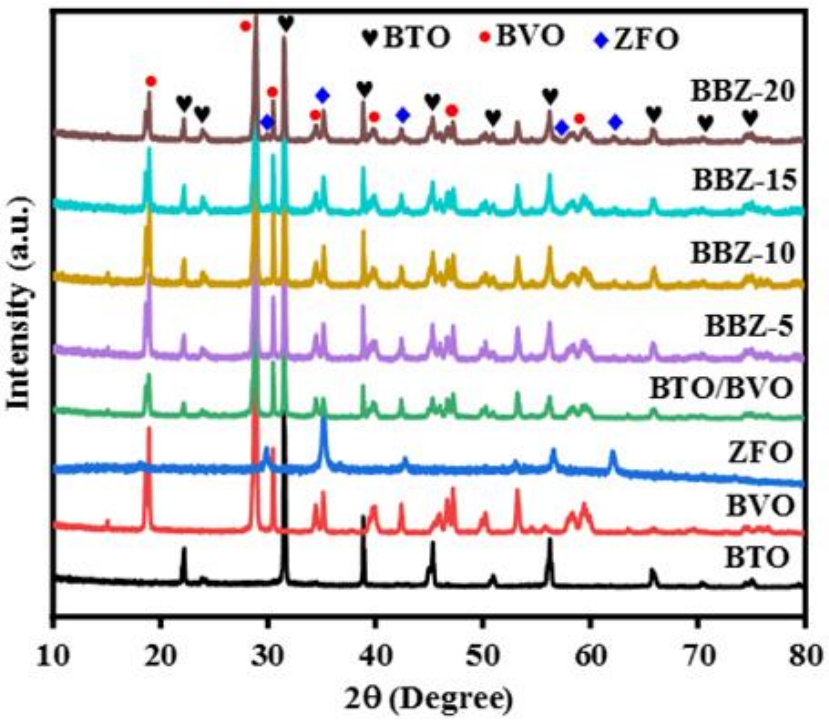

Fig. 1 XRD patterns of BTO, BVO, ZFO, BTO/BVO and BBZ ternary heterostructure

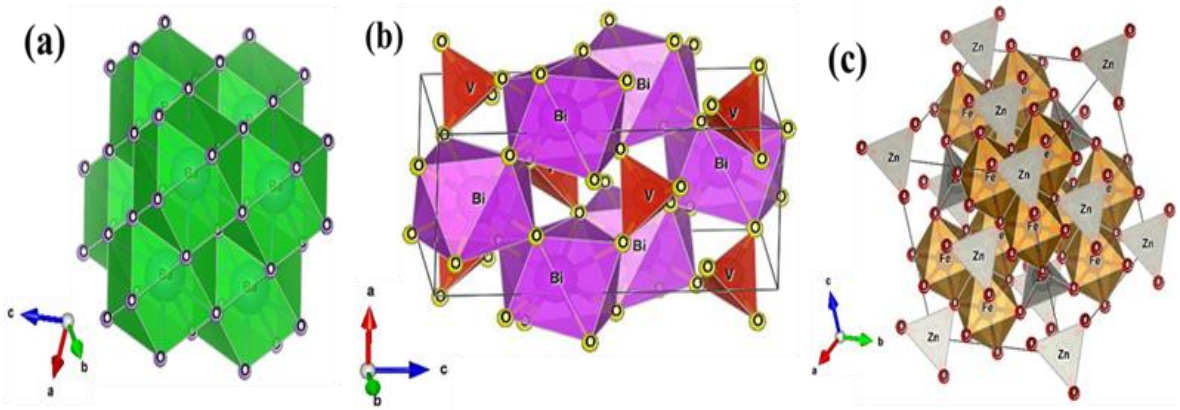

Fig. 2 Unit cell images of (a) BTO, (b) BVO and (c) ZFO by VESTA software

3.2 Fourier transform infrared spectroscopy (FTIR)

The FTIR spectra of pristine BTO, BVO, ZFO, BTO/BVO and their ternary nanocomposite are presented in Fig 3. As shown in Fig. 3(a), BTO exhibits a characteristic IR band at 430 cm^{-1} is attributed to the Ba-O bond [30]. The broad band at 546 cm^{-1} is ascribed as the Ti-O vibration within the $[TiO_6]^{-2}$ octahedron, conforming to its perovskite structure [31,32]. The peak observed at 856 cm^{-1} is associated with Ti-O-Ti bond vibrations [29]. Additionally, a band at 1448 cm^{-1} represents the Ba-Ti-O bond [33]. These findings indicate that the BTO formed without any impurities and was consistent with previous reports [22]. For BVO, (Fig. 3(b)), bands appear at 410, 476, 515 and 731 cm^{-1}. The bands at 410 and 476 cm^{-1} are assigned to the Bi-O bending vibrations [34], while the peak at 515 cm^{-1} is attributed to V-O-V deformation from the V-O stretching mode [35]. The broad band observed at 731 cm^{-1} is a characteristic peak of the VO_4^{-3} group in BVO [25]. The BTO/BVO binary nanocomposite (Fig. 3(c)) retains the characteristic IR bands of both BTO and BVO, confirming successful heterostructure formation.

The spectra of pure ZFO and the BBZ ternary composites are shown in Fig. 3(d)). For pristine ZFO, two well-defined bands at 338 and 403/605 cm^{-1} correspond to Fe-O and Zn-O stretching vibrations, respectively [36,37]. As the ZFO wt.% increases, the intensity of the 403 cm^{-1} absorption band shifts towards a higher wavenuber (blue shift), indicating strong interactions between BTO, BVO and ZFO. These observations confirm the successful formation of BBZ ternary nanocomposite.

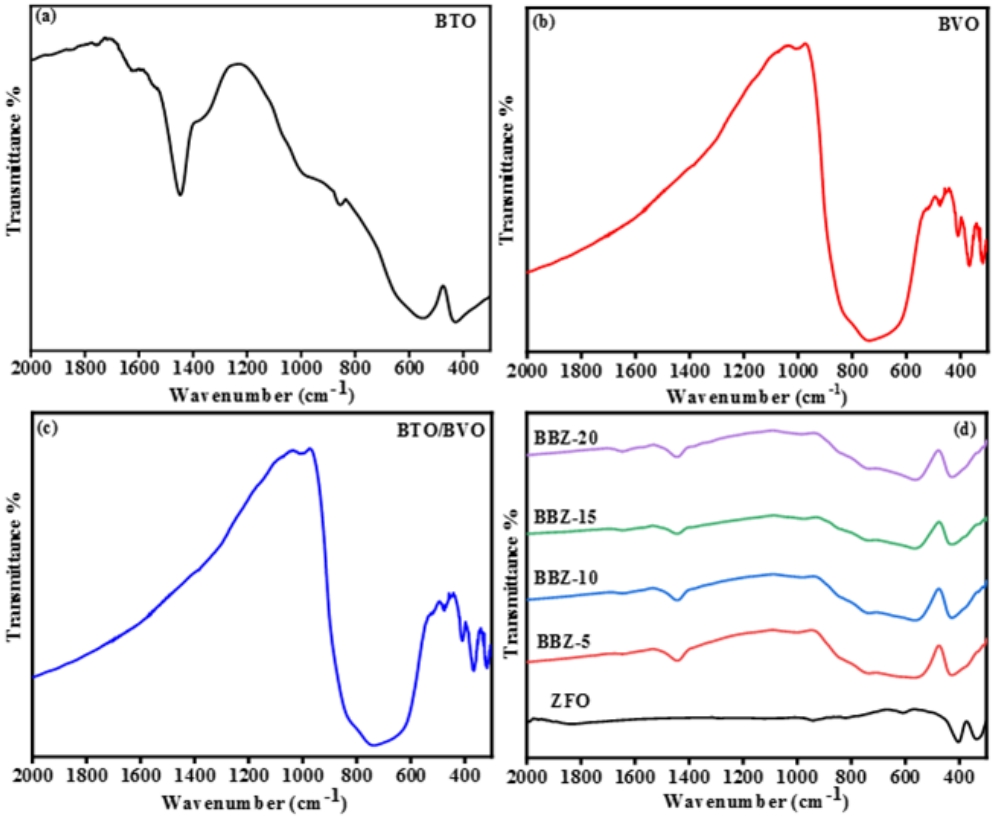

Fig. 3 FTIR spectra of (a) BTO, (b) BVO, (c) BTO/BVO, (d) ZFO and BBZ ternary composites

3.3 UV-Visible DRS

The band gap energy and light absorption properties of BTO, BVO, ZFO, BTO/BVO and their ternary heterojunctions were investigated using UV-visible DRS. The absorption edges of all nanocomposites are illustrated in Fig. 4(a) with values as follows: BTO (387.5 nm), BVO (529.91 nm), ZFO (620.79 nm), BTO/BVO (508.19 nm), BBZ-5 (626.12 nm), BBZ-10 (678.45 nm), BBZ-15 (669.01nm), and BBZ-20 (639.4 nm). Pure BTO shows an absorption in the ultraviolet region, while BVO incorporation shifts the absorption band to 508.19 nm. Further addition of ZFO (5, 10, 15, and 20 wt.%) to the BTO/BVO nanocomposite results in a progressive redshift. Among these, BBZ-10 exhibited the highest absorption, indicating optimal light-harvesting capability. However, as the ZFO content exceeds 10 wt.%, absorption decreases due to agglomeration, which hinders charge separation. These results suggest that 10 wt.% ZFO is the optimal composition for maximum dye degradation efficiency. The band gap energy (E_g) of all materials was determined using Tauc's plots of $(\alpha h\nu)^n$ versus E_g, as shown in Fig. 4(b), using the following equation [27].

$$(\alpha h\nu)^n = A(h\nu - E_g) \quad (4)$$

where α is the absorption coefficient, $h\nu$ is incident photon energy, A is a constant, E_g is the band gap energy, and n is the nature of the transition. For direct and indirect allowed transitions, the n values are 2 and 0.5 respectively. The E_g values are 3.2, 2.41, 1.83, 2.44, 2.80, 2.18, 2.20, and 2.31 eV for BTO, BVO, ZFO, BTO/BVO, BBZ-5, BBZ-10, BBZ-15 and BBZ-20, respectively.

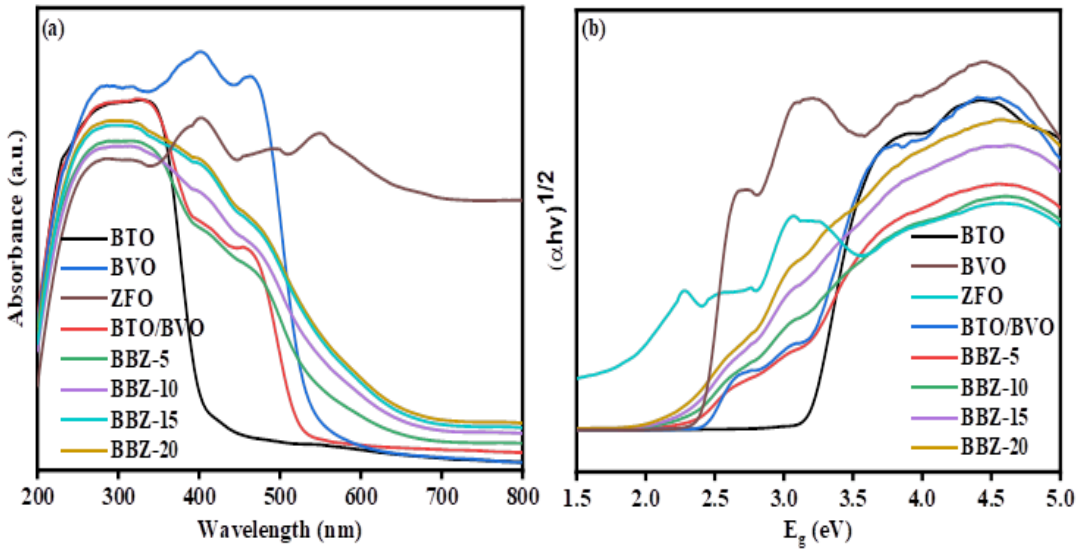

Fig. 4(a) UV-vis DRS spectra (b) Tauc's plots of BTO, BVO, ZFO, BTO/BVO, and BBZ composites.

3.4 FESEM-EDS

The morphology and microstructure of BTO, BVO, ZFO, BTO/BVO and BBZ-10 were determined from FESEM. As shown in Fig. 5(a), pure BTO exhibits cuboid-like structures along with some spherical shape particles, featuring smooth surfaces with diameters ranging from 50-70 nm [38–40]. The FESEM image of BVO (Fig. 5(b)) reveal a plate-like morphology with an average diameter of 120-180 nm and forming large aggregates of smooth particles [41–43]. As illustrated in Fig. 5(c), ZFO displays a granular particle morphology with an average particle size of 30-40 nm, consistent with previous references [44,45]. The FESEM micrograph of the BTO/BVO nanocomposite (Fig. 5(d)) shows a rough surface with tightly bonded BTO and BVO particles, maintaining distinct morphologies. In the FESEM image of the BBZ-10 ternary system (Fig. 5(e)), there is no significant morphological changes were observed compared to individual components, indicating successful heterostructure formation without structural distortion. The EDS spectrum of BBZ-10 confirms the presence of Ba, Ti, Bi, V, Zn, Fe and O elements as shown in Fig. 5(f), verifying the successful integration of all elements in the ternary heterostructure.

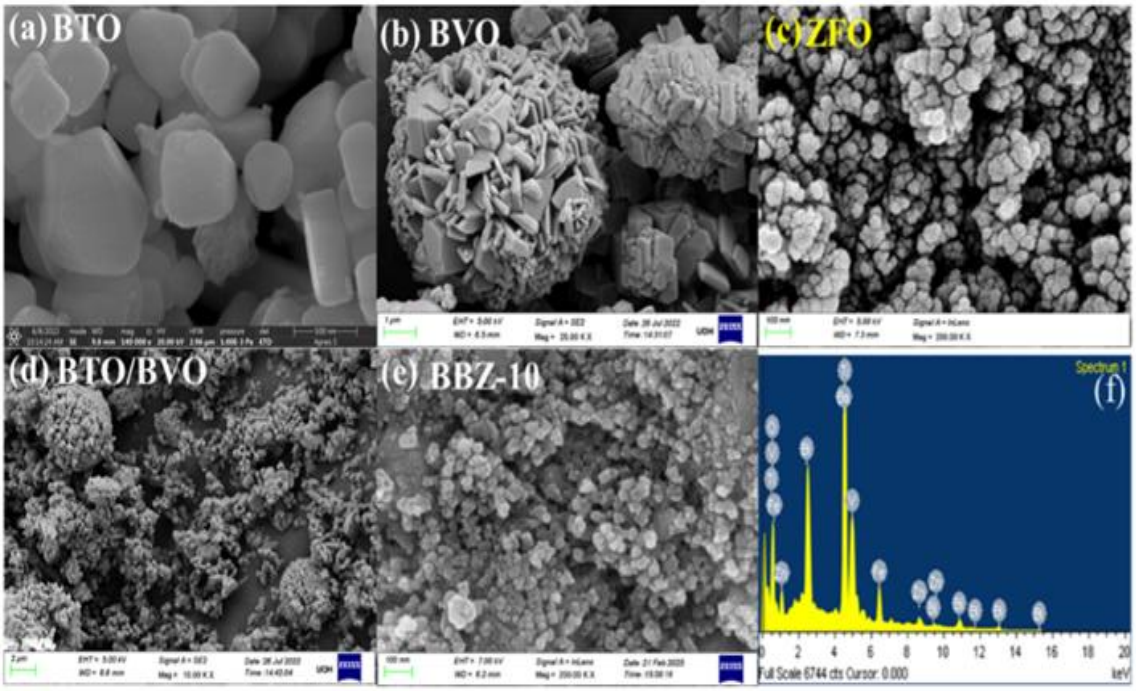

Fig. 5 FESEM images of (a) BTO, (b) BVO, (c) ZFO, (d) BTO/BVO, (e) BBZ-10 and (f) EDS spectrum of BBZ-10.

3.5 Photoluminescence (PL)

Photoluminescence (PL) analysis was used to investigate the charge transfer and recombination behaviour of photo-generated electron-hole pairs in the photocatalysts. In this study, PL spectra for BTO, BVO, ZFO, BTO/BVO and BBZ-10 composite were recorded at an excitation wavelength of 350 nm, as illustrated in Fig. 6(a). The pure BTO shows emissions in both UV and visible regions with a weak emission band at 390 nm attributed to electron-hole recombination and is observed due to charge transference from the Ti^{4+} ions to nearby O^{2-} ions within the TiO_6^{8-} octahedron. Additional peaks at 465 and 535 nm, as shown in the inset of Fig. 9(a), are attributed to intrinsic oxygen defects, and are supported by positron annihilation lifetime spectroscopy (PALS) [22]. Pure BVO shows the lowest PL intensity due to structural defects induced electron trapping [46,47]. The pristine ZFO displays a strong emission peak indicating a more charge recombination rate. Upon ZFO incorporation into the BTO/BVO composite, PL intensity decreases, suggesting improved effective charge separation compared to pristine ZFO [48]. This enhanced charge separation results in a higher availability of photogenerated charge carriers, thereby improving photocatalytic activity.

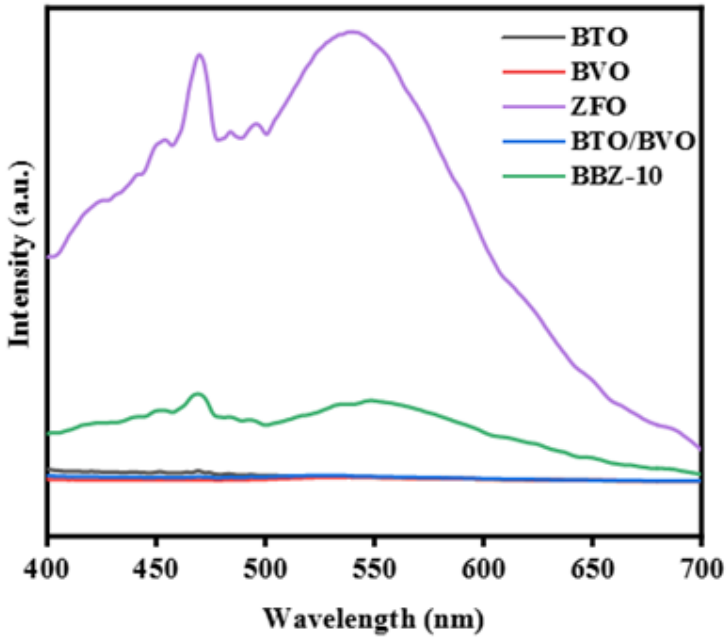

Fig. 6(a) PL spectra of BTO, BVO, ZFO, BTO/BVO and BBZ-10.

3.6 Photocatalytic activity (PCA)

The PCA of as-prepared BTO, BVO, ZFO, BTO/BVO and their nanocomposites were investigated under visible light irradiation, both with and without H_2O_2, for the degradation of MO dye. Fig. 7 illustrates the MO degradation efficiency in the absence of H_2O_2 and follows as: blank MO (3%), BTO (4.11%), BVO (5.71%), ZFO (7.6%), BTO/BVO (4.65%), ZFO-5 (9.39%), ZFO-10 (15%), ZFO-15 (10.14%), and ZFO-20 (9.2%). Upon addition of H_2O_2, (Fig. 8(a-d)) the photodegradation efficiencies increased to 14.9%, 24%, 37.4%, 54%, 21.3%, 31.9%, 82.4%, 52.8%, and 37.9% for MO, BTO, BVO, ZFO, BTO/BVO, BBZ-5, BBZ-10, BBZ-15, and BBZ-20, respectively (Fig. 8(b)). Among these, BBZ-10 exhibited the highest degradation efficiency, achieving 3.4 times the degradation of BTO and 3.86 times that of BTO/BVO. However, for BBZ-15 and BBZ-20, the degradation efficiency declined due to increased particle agglomeration, which can reduce light penetration. To further analyse the degradation process, a pseudo-first-order kinetic model was applied, with $\ln(C_0/C_t)$ plotted against irradiation time (Fig. 8(c)). The highest rate constant (0.00697 min^{-1}) was observed for BBZ-10, which was 5.05 times higher than that of pure BTO (0.00138 min^{-1}) and 5.40 times higher than the BTO/BVO binary system (0.00129 min^{-1}). The rate constants and degradation percentages of all the materials are summarized in Table 1. Additionally, the absorption spectra of MO in the presence of the BBZ-10 at different time intervals are depicted in Fig. 8(d). These results confirm that BBZ-10 demonstrates the highest photocatalytic performance among the BBZ ternary systems, significantly enhancing the degradation efficiency of pure BTO.

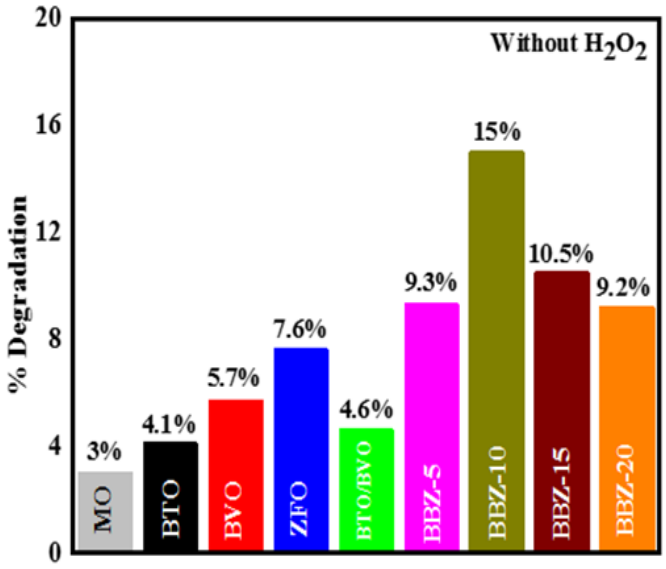

Fig. 7 Degradation% of MO with all the prepared compounds without H_2O_2.

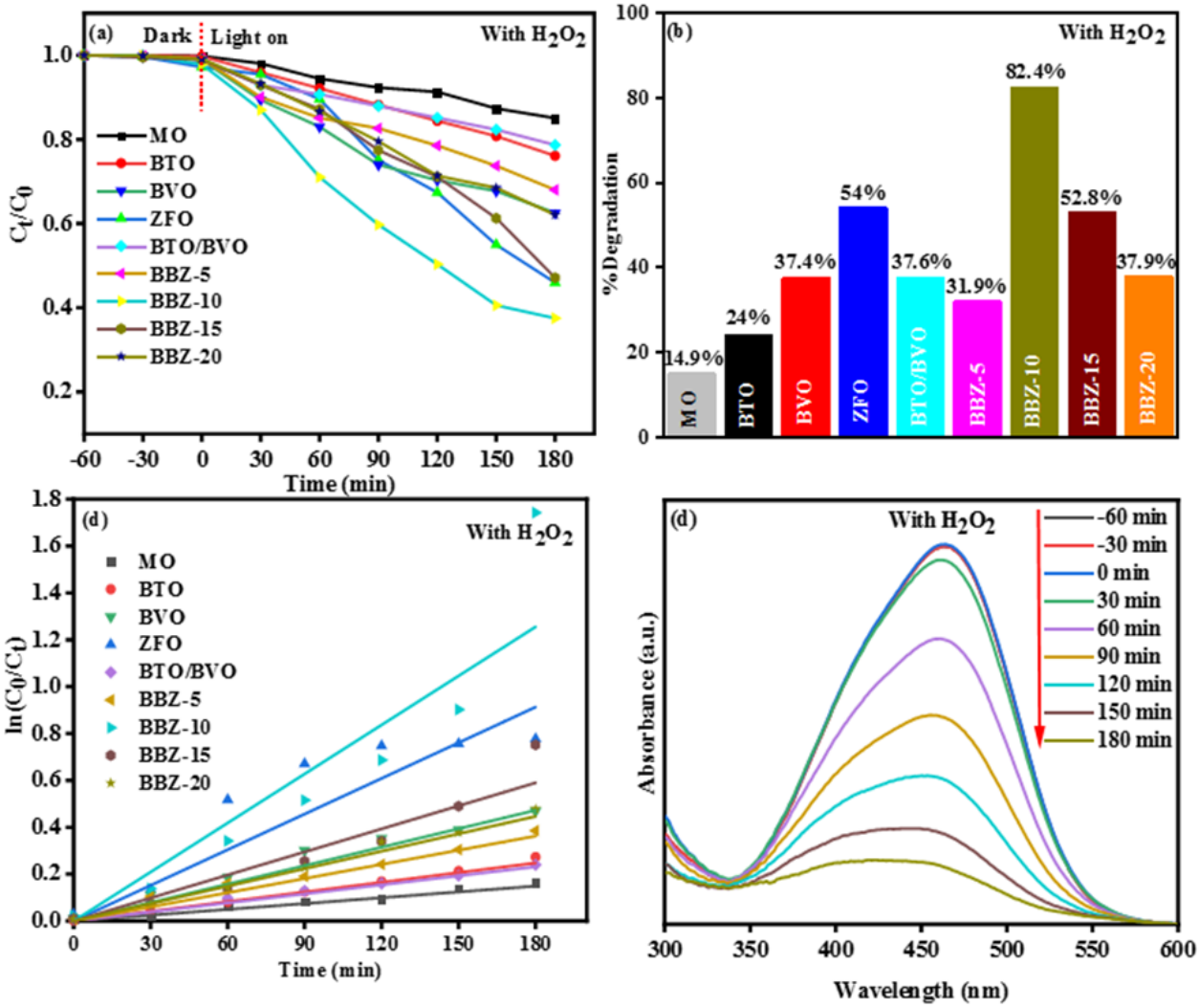

Fig. 8(a) Photodegradation profiles (b) % degradation (c) first-order kinetic plot of all the prepared compounds (d) absorption spectra of MO in the presence of BBZ-10 with H_2O_2.

3.6.1 PCA mechanism

The CB and VB edge potentials of BTO, BVO and ZFO are determined using the following equations.

$$E_{VB} = \chi - E_e + \frac{1}{2}E_g \quad (5)$$

$$E_{CB} = E_{VB} - E_g \quad (6)$$

The CB and VB potentials for BTO/BVO/ZFO are found to be -0.98/+0.45/-0.37 and +2.22/+2.86/+1.46 eV, respectively. The work function (Φ) values for BTO, BVO and ZFO are 4.8 [49–51], 5.27 [52,53], and 4.51 [18,54], respectively. As established, electrons naturally transfer from the materials with a lower Φ to those with a higher Φ. Figure 9(a) illustrates the work functions and fermi levels (E_f) of BTO, BVO and ZFO before contact. In the absence of light irradiation, when intimate interfaces are formed between BTO and BVO as well as between BVO and ZFO, electron migration occurs from BTO to BVO and from ZFO to BVO due to the higher fermi level of BTO and ZFO relative to BVO. Consequently, the interfaces near the BTO and ZFO regions become positively charged, while those near the BVO regions become negatively charged as illustrated in Fig. 9(b). The inner electric field at the double interfaces is established from the BTO to BVO and from the ZFO to BVO, respectively. The built-in electric fields can impede further electron migration until the fermi levels are aligned. Under light irradiation (Fig. 9(c)), BVO acts as an intermediary between BTO and ZFO, forming a dual S-scheme heterostructure. Electrons are transported from the CB of BVO to both BTO and ZFO through BTO-BVO and BVO-ZFO interfaces. The rapid transfer of electrons from the CB of BVO towards the VB bands of BTO and ZFO results in a greater gathering of electrons in the CB of BTO and ZFO and holes in the VB of BVO. These accumulated electrons in the CB of BTO and ZFO participate in the reduction process, converting O_2 into /$\bullet O_2^-$, due to their higher potential compared to the reduction potential of oxygen ($O_2/\bullet O_2^-$ is -0.33 eV vs NHE) [55,56]. Similarly, the accumulated holes in the VB of BVO can interact with H_2O or HO^- to generate hydroxyl radicals (•OH), as BVO has a sufficiently high VB potential (+2.86 eV vs NHE) as compared to the reduction potentials of $\bullet OH/H_2O$ (+2.68 eV vs NHE) [57,58]. Notably, the quantity of ZFO in the ternary system significantly influences the photodegradation of MO over the BBZ system. An excessive amount of ZFO potentially disrupt the PCA of the ternary system due to the varied surface area through more agglomeration. Based on the results the BBZ-10 hybrid photocatalyst demonstrates superior charge separation and efficient electron transfer via the dual S-scheme mechanism, leading to enhanced photocatalytic performance. The photodegradation mechanism of MO is as follows:

$$BTO + h\upsilon \longrightarrow BTO\ (e^-CB + h^+VB) \quad (7)$$

$$BVO + h\upsilon \longrightarrow BVO\ (e^-CB + h^+VB) \quad (8)$$

$$ZFO + h\upsilon \longrightarrow ZFO\ (e^-CB + h^+VB) \quad (9)$$

$$[BTO(e^-CB)/BVO\ (e^-CB)/ZFO\ (e^-CB)] + [BTO(h^+VB)/BVO\ (h^+VB)/ZFO\ (h^+VB)] \longrightarrow BTO\left[e^-CB^{total}\right] + BVO\left[h^+VB^{total}\right] + ZFO\left[e^-CB^{total}\right] \quad (10)$$

$$O_2 + e^-_{BTO.CB} \longrightarrow \bullet O_2^- \quad (11)$$

$$O_2 + e^-_{ZFO.CB} \longrightarrow \bullet O_2^- \quad (12)$$

$$H_2O + h^+ \rightarrow -OH + H^+ \quad (13)$$

$$H_2O_2 + e^-(CB) \rightarrow -OH + \bullet OH \quad (14)$$

$$H_2O_2 + h^+(VB) \rightarrow HOO^{\cdot} \quad (15)$$

$$HOO^{\cdot} + h^+ \rightarrow \bullet O_2^- \quad (16)$$

$$\bullet O_2^- + 2H^+ + e^- \rightarrow 2\bullet OH \quad (17)$$

$$\bullet OH\ \&\ \bullet O_2^- + MO \longrightarrow CO_2 + H_2O \quad (18)$$

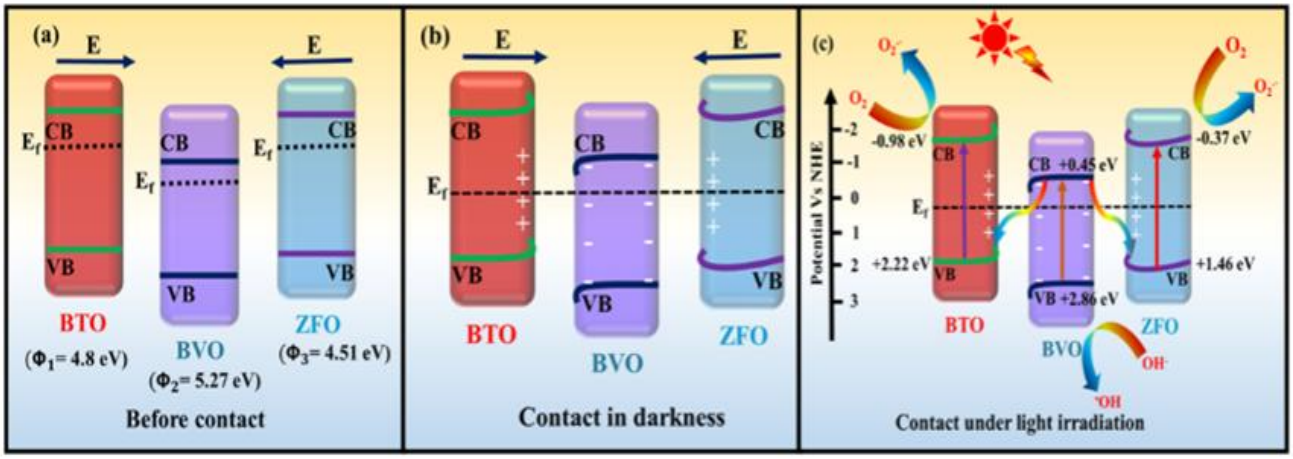

Fig. 9 Schematic representation of charge transfer in BTO/BVO/ZFO dual S-scheme heterojunction (a) Before contact, (b) Contact in darkness and (c) Contact under light irradiation.

Table 1 The photocatalytic rate constant (k), and % degradation values of MO with all the prepared compounds

Compounds	k (min^{-1})	%Degradation
MO	0.000827	14.9
BTO	0.00138	24
BVO	0.00263	37.4
ZFO	0.00507	52.1
BTO/BVO	0.00129	21.3
BBZ-5	0.00201	31.9
BBZ-10	**0.00697**	**82.4**
BBZ-15	0.00328	52.8
BBZ-20	0.0.00248	37.9

3.7 Recyclability and scavenger's experiment

To assess the stability of the BBZ-10 ternary system, a stability test was conducted by repeating the MO degradation experiment up to 4 times under similar conditions as depicted in Fig. 10(a). Remarkably, the PCA of the BBZ-10 showed any distinct deactivation even after 4 successive cycles. To distinguish the specific roles of active species, conducted a scavenger test. Ammonium Oxalate (AO), Benzo Quinone (BQ), and tertiary-Butyl alcohol (TBA) are utilized to quench the holes (h^+), superoxides ($\bullet O_2^-$) and hydroxyl radicals (•OH), respectively. The MO solution without scavenger and with BBZ-10 photocatalyst was degraded to 82.4%. When subjected to the addition of the above scavenger solutions the degradation percentages of all the samples are shown in Fig. 10(b). The hindrance rate of degradation was observed as follows: TBA (14%) > BQ (46.3 %) > AO (79.3%) > no scavenger (82.4%). The above results attributed that the $\bullet O_2^-$ and •OH are responsible for the enhancement of PCA of the BBZ-10 ternary system.

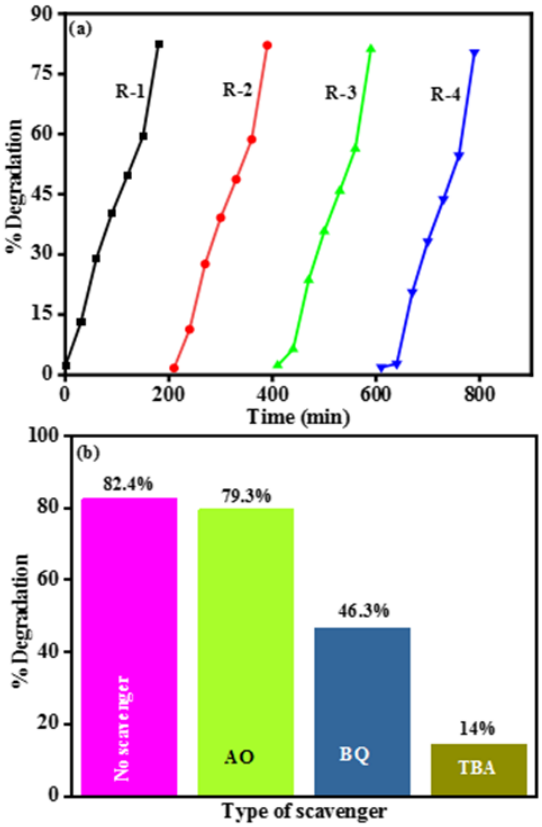

Fig. 10(a) Recyclability and (b) Scavengers test for BBZ-10.

IV. Conclusions

In summary, the successful fabrication of the BTO/BVO/ZFO ternary system has been achieved. XRD and FESEM analyses confirm the presence of BTO, BVO, ZFO and their composites. FTIR analyses the formation of heterostructures and chemical interactions at their interfaces. UV-visible DRS investigations reveal the broader visible light absorption of BBZ-10 compared to pristine compounds, favouring improved photocatalytic activity. The BBZ-10 heterojunction exhibits significantly enhanced photocatalytic activity through a dual S-scheme mechanism for MO degradation. The superior photodegradation of the BBZ-10 ternary system is attributed to the synergistic effect between the well-corresponding redox potential edges of BTO, BVO and ZFO and low charge recombination. PL studies further demonstrate reduced recombination of charge carriers of BBZ-10. The superoxides $\bullet O_2^-$ and hydroxyl radicals (•OH) are responsible for the degradation of MO.

References

[1] B.J. Kim, C.S. Gee, Water Environ. Res. 65 (1993) 430–441.
[2] G. Mishra, M. Tripathy, Colourage 40 (1993) 35.
[3] T. Shahwan, S.A. Sirriah, M. Nairat, E. Boyacı, A.E. Eroğlu, T.B. Scott, K.R. Hallam, , Chem. Eng. J. 172 (2011) 258–266.
[4] J. Low, J. Yu, M. Jaroniec, S. Wageh, A.A. Al-Ghamdi, Adv. Mater. 29 (2017) 1601694.
[5] S. Asadzadeh-Khaneghah, A. Habibi-Yangjeh, J. Clean. Prod. 276 (2020) 124319.
[6] D. Huang, X. Yan, M. Yan, G. Zeng, C. Zhou, J. Wan, M. Cheng, W. Xue, ACS Appl. Mater. Interfaces 10 (2018) 21035–21055.
[7] H. Wang, L. Zhang, Z. Chen, J. Hu, S. Li, Z. Wang, J. Liu, X. Wang, Chem. Soc. Rev. 43 (2014) 5234–5244.
[8] Q. Xu, L. Zhang, B. Cheng, J. Fan, J. Yu, Chem 6 (2020) 1543–1559.
[9] K. Zhang, Y. Li, S. Yuan, L. Zhang, Q. Wang, Wuli Huaxue Xuebao/ Acta Phys. Chim. Sin. 39 (2023) 1–18.
[10] Q. Xu, L. Zhang, B. Cheng, J. Fan, J. Yu, 6 (2020) 1543–1559.
[11] D. Zhong, W. Liu, P. Tan, A. Zhu, Y. Liu, X. Xiong, J. Pan, Appl. Catal. B Environ. 227 (2018) 1–12.
[12] M. Ali, R. Singh, R. Kumari, D. Guin, C.S.P. Tripathi, Mater. Sci. Semicond. Process. 178 (2024) 108454.
[13] X. Zhou, X. Wang, T. Tan, H. Ma, H. Tang, X. Luo, F. Dong, Y. Yang, Chem. Eng. J. 470 (2023) 143933.
[14] X. Liu, Y. Li, P. Li, Colloids Surfaces A Physicochem. Eng. Asp. 686 (2024) 133411.
[15] M. Song, J. He, Y. Liu, Y. Wu, Y. Su, J. Environ. Chem. Eng. 12 (2024) 113300.
[16] Y.W. Li, S.Z. Li, M. bo Zhao, W.L. Ma, Sep. Purif. Technol. 327 (2023) 124966.
[17] Z. Xu, C. Qin, J. Zhong, S. Huang, M. Li, S. Zhang, H. Yang, L. Ma, Solid State Sci. 129 (2022) 106908.
[18] A. Behera, D. Kandi, S. Sahoo, K. Parida, J. Phys. Chem. C 123 (2019) 17112–17126.
[19] Y. Zhao, H. Yang, H. Hao, F. Zhu, G. Zhang, J. Bi, S. Yan, H. Hou, Langmuir 38 (2022) 13437–13447, https://doi.org/10.1021/acs.langmuir.2c01881.
[20] H. Tang, R. Li, X. Fan, Y. Xu, H. Lin, H. Zhang, J. Environ. Chem. Eng. 10 (2022) 107797.
[21] D.A. Sabit, S.E. Ebrahim, Z.H. Jabbar, J. Photochem. Photobiol. A Chem. 443 (2023) 114849.
[22] G. Swarupa, N. Anuradha, K. Narsimha, K. Sudarshan, G. Upender, B. Vijaya Kumar, Mater. Sci. Semicond. Process. 182 (2024) 108715.
[23] M. Yan, Y. Wu, Y. Yan, X. Yan, F. Zhu, Y. Hua, W. Shi, ACS Sustain. Chem. Eng. 4 (2016) 757–766.
[24] W. Ma, N. Wang, L. Yang, M. Lv, Z. Zhu, S. Li, J. Mater. Sci. Mater. Electron. 31 (2020) 8761–8772.
[25] Q. Yang, S. Wei, L. Zhang, R. Yang, New J. Chem. 44 (2020) 17641–17653.
[26] I. Khan, S. Ali, M. Mansha, A. Qurashi, Ultrason. Sonochem. 36 (2017) 386–392.
[27] X. He, C. Zhang, D. Tian, Materials (Basel). 13 (2020) 1628.
[28] X. Wu, J. Lu, S. Huang, X. Shen, S. Cui, X. Chen, Appl. Surf. Sci. 594 (2022) 153486.
[29] K. V. Alex, A. Prabhakaran, A.R. Jayakrishnan, K. Kamakshi, J.P.B. Silva, K.C. Sekhar, ACS Appl. Mater. Interfaces 11 (2019) 40114–40124.
[30] X. Zhang, X. Wang, J. Chai, S. Xue, R. Wang, L. Jiang, J. Wang, Z. Zhang, D.D. Dionysiou, Appl. Catal. B Environ. 272 (2020) 119017.
[31] M.A.M. Khan, S. Kumar, J. Ahmed, M. Ahamed, A. Kumar, ceramics, Mater. Chem. Phys. 259 (2021) 124058.
[32] Y. Wang, H. Yang, X. Sun, H. Zhang, T. Xian, Mater. Res. Bull. 124 (2020) 110754.
[33] S. Kappadan, T.W. Gebreab, S. Thomas, N. Kalarikkal, Mater. Sci. Semicond. Process. 51 (2016) 42–47.
[34] M. Mousavi-Kamazani, J. Mater. Sci. Mater. Electron. 30 (2019) 17735–17740.
[35] M.M. Sajid, S.B. Khan, N.A. Shad, N. Amin, Z. Zhang, RSC Adv. 8 (2018) 23489–23498.
[36] O.D. Maynez-Navarro, M.A. Mendez-Rojas, D.X. Flores-Cervantes, U.S. Kuri, J.L. Sanchez-Salas, ChemistrySelect 5 (2020) 15167–15174.
[37] Ikramullah, N. Ali, F. Ali, Z.A. Sheikh, M. Bilal, I. Ahmad, Water. Air. Soil Pollut. 231 (2020) 1–12.
[38] N.K. Veldurthi, N. KrishnaRao Eswar, S.A. Singh, G. Madras, Int. J. Hydrogen Energy 43 (2018) 22929–22941.
[39] S. Selvarajan, P. Malathy, A. Suganthi, M. Rajarajan, J. Ind. Eng. Chem. 53 (2017) 201–212.
[40] T. Xian, H. Yang, L.J. Di, J.F. Dai, J. Alloys Compd. 622 (2015) 1098–1104.
[41] B. Samran, S. lunput, S. Tonnonchiang, S. Chaiwichian, Phys. B Condens. Matter 561 (2019) 23–28.
[42] Y. Wang, J. Niu, X. Gao, Y. Zhang, Appl. Surf. Sci. 533 (2020) 147458.
[43] C. Qin, S. Lei, X. Tang, J. Zhong, J. Li, J. He, Inorg. Chem. Commun. 116 (2020) 107904.
[44] P. Chen, J. Sol-Gel Sci. Technol. 82 (2017) 397–406.
[45] R. Roshani, A. Tadjarodi, J. Mater. Sci. Mater. Electron. 31 (2020) 23025–23036.
[46] P. Praus, J. Lang, A. Martaus, L. Svoboda, V. Matějka, M. Kormunda, M. Šihor, M. Reli, K. Kočí, J. Inorg. Organomet. Polym. Mater. 29 (2019) 1219–1234.
[47] L.A.T. Hoang, N. Le-Duy, T.D. Nguyen, T. Lee, ChemistrySelect 8 (2023) 1024.
[48] Y. Liu, H. Ren, H. Lv, J. Guang, Y. Cao, Appl. Surf. Sci. 433 (2018) 610–616.
[49] D.G. Popescu, M.A. Husanu, C. Chirila, L. Pintilie, C.M. Teodorescu, Appl. Surf. Sci. 502 (2020) 144101.
[50] D.G. Popescu, M.A. Husanu, C. Chirila, L. Pintilie, C.M. Teodorescu, Phys. Status Solidi - Rapid Res. Lett. 13 (2019) 3–7.
[51] T. Schulmeyer, S.A. Paniagua, P.A. Veneman, S.C. Jones, P.J. Hotchkiss, A. Mudalige, J.E. Pemberton, S.R. Marder, N.R. Armstrong, J. Mater. Chem. 17 (2007) 4563–4570.
[52] M. Mehta, S. Krishnamurthy, S. Basu, T.P. Nixon, A.P. Singh, Mater. Today Chem. 17 (2020) 100283.
[53] Y. Lin, D. Pan, H. Luo, Mater. Sci. Semicond. Process. 121 (2021) 105453.
[54] A. Behera, D. Kandi, S. Martha, K. Parida, Inorg. Chem. 58 (2019) 16592–16608.

[55] Q. Wan, T.H. Wang, J.C. Zhao, Appl. Phys. Lett. 87 (2005) 19–21.
[56] N. P.M, L.G. Devi, 16 (2020) 100411. https://doi.org/10.1016/j.surfin.2019.100411.
[57] B. Wang, K. Wei, F. Chen, Y. Wang, G. He, W. Li, J. Liu, Q. He, J. Alloys Compd. 804 (2019) 100–110.
[58] J. Xiao, Y. Xie, H. Cao, Y. Wang, Z. Zhao, Catal. Commun. 66 (2015) 10–14.